










Environmental sub-MeV neutron measurement at the Gran Sasso surface laboratory with a super-fine-grained nuclear emulsion detector

T. Shiraishi ^{1,*}, S. Akamatsu,¹ T. Naka ^{1,2}, T. Asada ^{3,4}, G. De Lellis ^{3,5}, V. Tioukov ⁵, G. Rosa,⁶ R. Kobayashi ⁷,
N. D'Ambrosio ⁴, A. Alexandrov ^{3,5} and O. Sato ⁸

¹Department of Physics, Toho University, Chiba J-274-8510, Japan

²Kobayashi-Maskawa Institute for the Origin of Particles and the Universe, Nagoya University, Aichi J-464-8602, Japan

³Università degli studi di Napoli "Federico II", Napoli I-80126, Italy

⁴Laboratori Nazionali del Gran Sasso - INFN, L'Aquila I-67100, Italy

⁵Istituto Nazionale di Fisica Nucleare, Napoli I-80126, Italy

⁶Sezione INFN di Roma, Roma I-00185, Italy

⁷Graduate School of Science, Nagoya University, Aichi J-464-8602, Japan

⁸Institute of Materials and Systems for Sustainability, Nagoya University, Aichi J-464-8602, Japan



(Received 22 September 2022; accepted 29 November 2022; published 10 January 2023)

The measurement of environmental neutrons is particularly important in the search for new physics, such as dark matter particles, because neutrons constitute an often irreducible background source. The measurement of the neutron energy spectra in the sub-MeV scale is technically difficult because it requires a very good energy resolution and a very high γ -ray rejection power. In this study, we used a super-fine-grained nuclear emulsion, called nano imaging tracker, as a neutron detector. The main target of neutrons is the hydrogen (proton) content of emulsion films. Through a topological analysis, proton recoils induced by neutron scattering can be detected as tracks with submicrometric accuracy. This method shows an extremely high γ -ray rejection power, at the level of $5 \times 10^7 \gamma/\text{cm}^2$, which is equivalent to five years accumulation of environmental γ rays, and a very good energy and direction resolution even in the sub-MeV energy region. In order to carry out this measurement with sufficient statistics, we upgraded the automated scanning system to achieve a speed of 250 g/(year machine). We calibrated the detector performance of this system with 880 keV monochromatic neutrons: a very good agreement with the expectation was found for all the relevant kinematic variables. The application of the developed method to a sample exposed at the INFN Gran Sasso surface laboratory provided the first measurement of sub-MeV environmental neutrons with a flux of $(7.6 \pm 1.7) \times 10^{-3} n/(\text{cm}^2 \text{ s})$ in the proton energy range between 0.25 and 1 MeV (corresponds to neutron energy range between 0.25 and 10 MeV), consistent with the prediction. The neutron energy and direction distributions also show a good agreement.

DOI: [10.1103/PhysRevC.107.014608](https://doi.org/10.1103/PhysRevC.107.014608)

I. INTRODUCTION

Environmental neutrons are normally a background source for experiments searching for dark matter and neutrinoless double- β decay in underground laboratories. Therefore, the measurement of their properties including the relative abundance is particularly important for these searches. For a weakly interacting massive particle (WIMP) [1,2] in the $1-10^4 \text{ GeV}/c^2$ mass range, the Maxwell-Boltzman distribution of its velocity in the Milky Way galaxy corresponds to nuclear recoil energies in the 1–10 keV range. Sub-MeV neutrons would produce nuclear recoils with similar energies and therefore their investigation is particularly important for the WIMP search.

Environmental neutrons in the sub-MeV region have not been directly measured owing to technical difficulties. In 1988, the measurement of environmental neutrons was carried

out by Rindi *et al.* at the INFN Laboratori Nazionali del Gran Sasso (LNGS) [3]. They used an ^3He proportional counter, particularly suited for the measurement of thermal neutrons. However, this device detects protons produced by the neutron absorption reaction $^3\text{He}(n, p)^3\text{H}$, once the neutrons are decelerated by a moderator. Therefore, a large systematic uncertainty is introduced in the energy resolution by the moderator, which prevents the energy reconstruction for sub-MeV neutrons. Moreover, the detector is not sensitive to the direction of the neutrons since the spatial resolution is not adequate.

We have developed a new direct detection method for neutrons with energies down to the sub-MeV domain [4], by using a super-fine-grained nuclear emulsion, called nano imaging tracker (NIT) [5,6]. Owing to its unprecedented spatial resolution at the nanometric scale, this device provides the three-dimensional (3D) reconstruction of proton tracks induced by the neutron scattering, thus being sensitive to the sub-MeV neutron energy region and providing measurements of both the neutron energy and direction. Moreover, it provides a very high γ -ray rejection power and it is capable

*takuya.shiraishi@sci.toho-u.ac.jp

of detecting and measuring neutrons even in an environment with a high γ -ray rate.

This study is meant to demonstrate the capability of measuring the neutron energy and direction in the sub-MeV domain, by detecting those environmental neutrons at the LNGS surface laboratory. In the first part of this work we report about the upgrade of the automated scanning system, to make it faster and collect a larger statistical sample. The performance of the system in the neutron detection was carefully measured by using monochromatic neutrons in the sub-MeV region. We then report the results of the environmental neutron measurements at the LNGS surface laboratory: the neutron flux and its directional distributions in the sub-MeV region are provided. Finally, we discuss the potential of this detection technique for future underground environmental neutron measurements and to search for proton recoils induced by light dark matter scattering.

II. DETECTION TECHNIQUE

A. Nano imaging tracker

NIT is a super-high-resolution nuclear emulsion [5,6] developed for the NEWSdm experiment [7], designed to search for dark matter through the direct detection of the induced nuclear recoils, for the first time with a directional sensitive approach. NIT consists of AgBr:I crystals of several tens of nanometers dispersed in a medium made of gelatin and polyvinyl alcohol: each crystal acts as the sensor of charged particles. In this study, we used the NIT type with (70 ± 10) nm AgBr:I crystals, dispersed with a density of about 2000 crystals/ μm^3 , producing an overall mass density of (3.2 ± 0.2) g/ cm^3 .

NIT contains various nuclear targets such as Ag, Br, C, N, O, and H. For the neutron detection, hydrogen acts as the leading target given the larger recoil energy transfer. The hydrogen mass fraction is $(1.75 \pm 0.30)\%$. The small size of AgBr:I crystals turns into a large energy deposition per unit length (few 10 keV/ μm) required to sensitize the crystal. This makes NIT insensitive to electrons, except at their stopping point, and thus γ rays do not provide a signal track. It makes this neutron detection approach γ -ray background free.

Nuclear emulsion is usually handled in the form of films, obtained by pouring an emulsion sensitive layer of up to several hundreds μm on a mechanical support, known as a base, made of plastic or glass. In this study, we used cyclo olefin polymer (COP) as the base material, due to its low radioactivity from ^{238}U and ^{232}Th , and to its high light transmittance, particularly important in the observation at an epioptical microscope. For the COP base, ZEONOR[®] by ZEON Corporation was selected. The maximum size of the COP base is 120 mm \times 100 mm with a thickness of 2 mm. The NIT emulsion was purified with a 0.22 μm PES filter (Millex[®]-GP from the Merck company) to remove dust, and it was poured as a 65 μm -thick sensitive layer on a COP base of 100 mm \times 80 mm size. A thin gelatin layer with 40 nm silver nanoparticles dispersed was applied to the top and bottom as a marker to recognize the emulsion layer.

TABLE I. Upgraded specification of PTS for the chain tracking system.

	Previous Work [4]	Current System
Objective Lens	N.A. 1.45, 100 \times	N.A. 1.42, 66.8 \times
Camera Pixel Pitch	5.5 μm	7.0 μm
Pixel Resolution	0.055 μm	0.105 μm
Number of Pixels	2048 \times 1088	2304 \times 1720
Camera Frame Rate	300 fps	500 fps
FOV	112 μm \times 60 μm	241 μm \times 180 μm
Image Processor	CPU	GPU
Scanning Speed	30	250
[g/(year machine)]		

The sensitization and development process of NIT is similar to that already described in a previous neutron study [4]. However, due to the larger thickness used for this work, during the fixing treatment at room temperature, NIT samples were soaked for approximately 1.5 h until the dissolution was confirmed by eye inspection. After this treatment, NIT got shrunk by a factor (0.61 ± 0.04) with respect to the original thickness. This factor is accounted for during the analysis at the microscope.

B. Three-dimensional submicrometric tracking system

For the NIT analysis, we have developed a three-dimensional submicrometric tracking method called chain tracking [4], by using the scanning system denoted as post track selector (PTS) [8,9], as shown in Fig. 1. The chain tracking is a proprietary 3D track reconstruction algorithm for the tomographic image acquired by the PTS. It first creates pairs of neighboring silver grains produced by the passage of charged particles, then recursively connects, with a chainlike structure, all patterns produced by other silver grains falling within the angular and position allowance. It finally selects the longest chain as a track. This enables automated analysis of tracks longer than 2 μm with a well-assessed detection efficiency. With this cut on the track length, γ rays do not produce detectable tracks, because NIT is sensitive to electrons induced by γ rays only at their stopping point. However, the chance coincidence of two γ rays has to be considered during a long run when the γ -ray density increases. We made a dedicated γ -ray exposure by using an ^{241}Am source with a density of 5×10^7 γ/cm^2 , equivalent to the amount of environmental γ rays integrated along five years. No evidence was found for track candidates induced by γ rays, which excluded the background from this source.

For all candidate tracks detected by the chain tracking, the coordinates (X, Y, Z) of the center of brightness for the two most distant developed silver grains are defined as start and end points, such that the 3D track range and direction are calculated thereafter.

We have upgraded the objective lens of the microscope. Indeed, in the previous setup, the 100 \times objective lens showed a pixel of 0.055 μm , an oversampling compared to the point spread of about 0.25 μm due to the diffraction limit. Table I shows the objective lens and camera used in the current

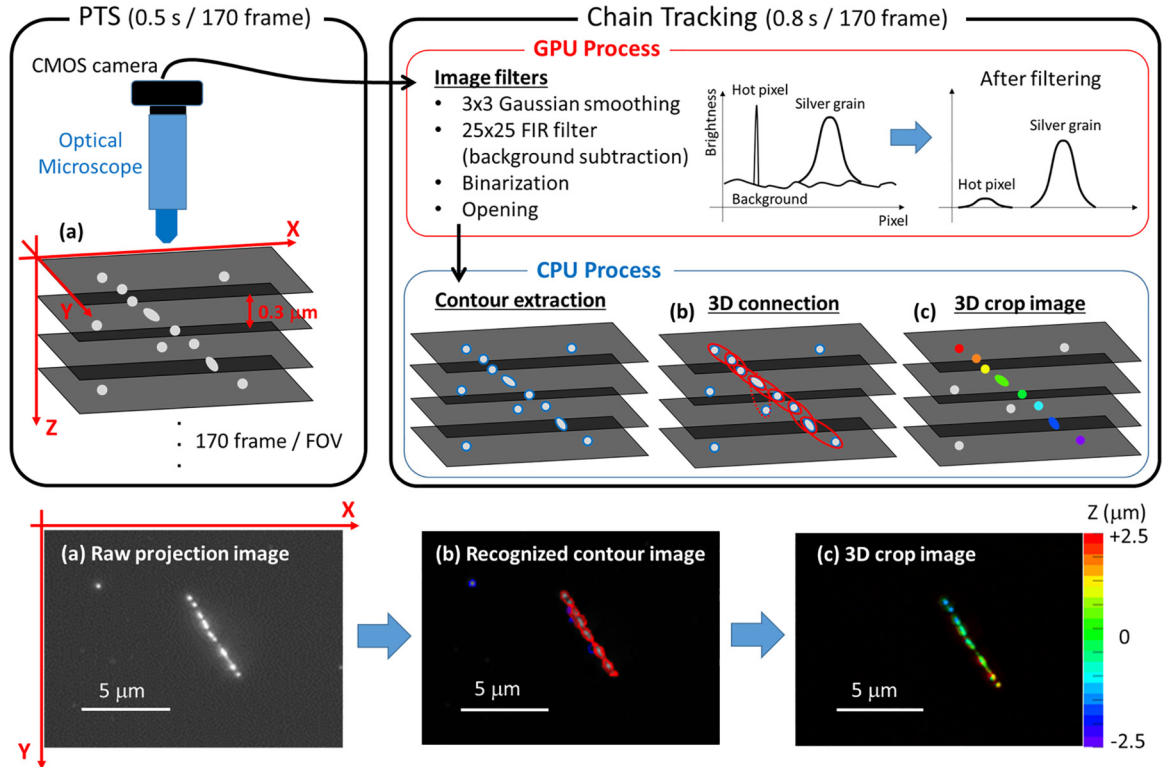


FIG. 1. Analysis flow of the 3D track reconstruction algorithm, denoted as chain tracking, for tomographic images acquired by the PTS. (a) Projection in the Z direction of 170 frames of tomographic images. After performing a Gaussian smoothing and a background subtraction in each frame with a GPU-based processing, the contours of the developed silver grains are extracted and a 3D connection is performed on the CPU. The recognized track is shown in red (b). Finally, a 3D crop image displays the Z coordinate with a colored scale (c).

microscope setup: this corresponds to a wider field of view (FOV) with a lower sampling pitch and a faster scanning speed. Furthermore, the image analysis in the current setup is performed by a GPU (GeForce RTX 2080 Ti) stream processing to accelerate image filtering, rather than by the CPU parallel processing. Consequently, the analysis speed of the PTS with the chain tracking system has achieved 250 g/(year machine), instead of 30 g/(year machine) [4]. In addition, the algorithm was upgraded and optimized to reduce the uncertainty on the 3D range measurement due to misconnections in the automated analysis.

The depth of field determining the accuracy of this optical system in the direction perpendicular to the film surface (Z direction) is approximately $0.3 \mu\text{m}$. When acquiring a tomographic image in the Z direction, the optical system moves at a speed of $0.3 \mu\text{m}/\text{frame}$ to perform continuous imaging with the camera. During scanning, the emulsion shrunk to approximately $40 \mu\text{m}$, and 170 frames (equivalent to $51 \mu\text{m}$) are acquired in the Z direction for each FOV.

III. DETECTOR CALIBRATION BY MONOCHROMATIC NEUTRON

In this section, we describe the evaluation of detection performance using monochromatic sub-MeV neutrons generated from a fusion reaction at the National Institute of Advanced Industrial Science and Technology (AIST) [10]. For the recoil protons detected by the chain tracking, the three-dimensional

range R [μm] and the scattering angle θ_{Scat} are measured, and the correlation between the proton range and energy E_p (MeV) in the NIT is approximated as it follows:

$$E_p \approx 0.045 + 0.539 \times \sqrt{R} - 0.446 \times \sqrt[3]{R} \quad (\text{MeV}). \quad (1)$$

The neutron energy E_n in elastic scattering with the proton can be derived from the following equation:

$$E_n = \frac{(m_n + m_p)^2}{4m_n m_p} \frac{E_p}{\cos^2 \theta_{\text{Scat}}} \approx \frac{E_p}{\cos^2 \theta_{\text{Scat}}}, \quad (2)$$

where we used the approximation $m_n \simeq m_p$, with m_n and m_p the neutron and proton masses, respectively.

In a previous work [4], we reported that the energy measurement through Eq. (2) showed an accuracy of $\Delta E_{n,\text{FWHM}}/E_n = 0.42$ for 540 keV neutrons. In this study, we have redone the calibration with monochromatic sub-MeV neutrons to check the effect on the measurement accuracy induced by the upgrade of the optical microscope, and to verify the accuracy obtained through the automated measurement by the chain tracking algorithm. In addition, NIT detector was kept at low temperature to suppress thermal noise and prevent the fading of latent image during long-term measurements. Therefore, we have also prepared a new neutron exposure to check the sensitivity of NIT films to protons at -26°C .

We used the monochromatic neutrons produced from the ${}^3\text{H}(p, n){}^3\text{He}$ reaction by bombarding a tritium-titanium layer evaporated on a 0.5 mm thick copper backing with a

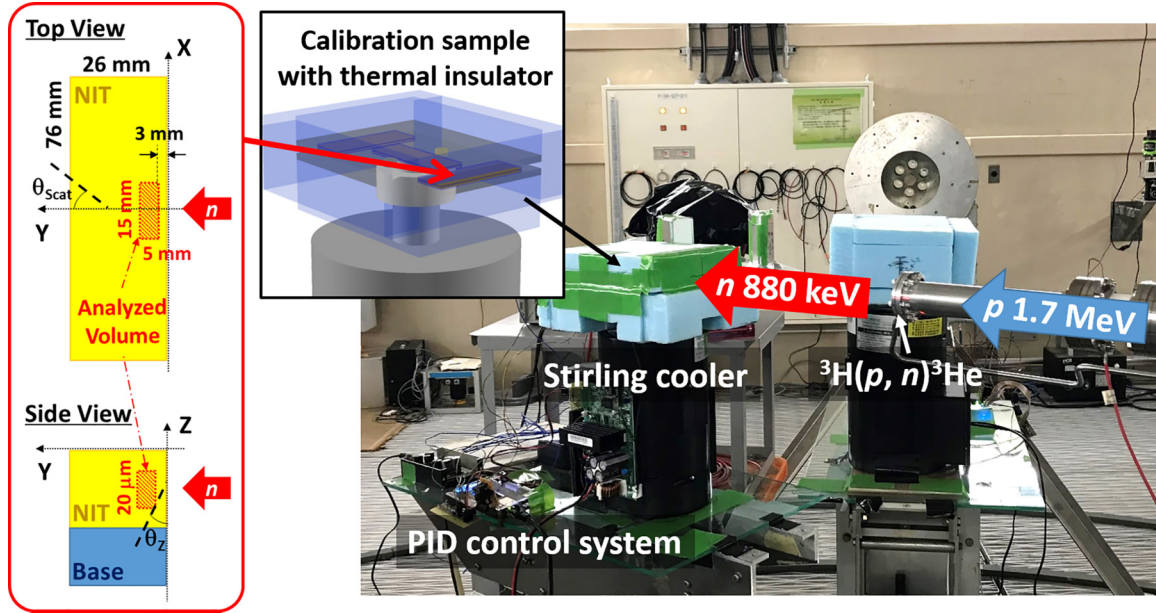


FIG. 2. Setup of the exposure of NIT films to a monochromatic neutron beam produced through the ${}^3\text{H}(p, n){}^3\text{He}$ reaction with a 1.7 MeV proton beam at AIST.

1.7 MeV proton beam from the 4 MV Pelletron accelerator at AIST [10]. Neutrons emitted in this reaction at an angle of 0° have an energy $E_n = 880 \pm 20$ keV, and the total flux after 7.88 h exposure was $(4.75 \pm 0.26) \times 10^7$ n/cm^2 at the sample location (32 cm away from the neutron source), as measured by the BF_3 proportional counter. NIT films were placed in a way to have their surface parallel to the incoming neutrons. A portable cooling system using a Stirling cooler and a PID control system (see Appendix A) was used to keep the temperature stable at -26°C during the exposure. Figure 2 shows the setup used for the neutron exposure.

In order to evaluate the accuracy in the range measurement by the automatic chain tracking algorithm, a comparison track by track with manual measurements was performed, as shown in Fig. 3. The automated measurement has an error of approximately $0.2 \mu\text{m}$ compared to the manual measurement, which turns into an uncertainty of approximately 20 keV for the proton energy, sufficient to explore the sub-MeV energy spectrum.

In order to evaluate the detection efficiencies, we have made a full simulation of the setup used for the 880 keV monochromatic neutron exposure. The simulation of the neutron propagation relies on GEANT4 libraries: G4HadronElasticPhysicsHP and G4HadronPhysicsShielding for the neutron scattering model, and G4EmLivermore for the electromagnetic model. We have included in the simulation the description of all the surrounding materials close to the NIT sample, such as the sample mounting and the Stirling cooler. The neutron flux and its energy spectrum were simulated for each neutron emission angle, and the tracking pitch for recoil protons in the NIT was set at $0.1 \mu\text{m}$. In order to avoid the uncertainty associated with the neutron attenuation induced by the scattering, the comparison was done in the proximity of the neutron incident position on the NIT sample. The simulation was normalized to the data, accounting for the

actual number of incoming neutrons during the exposure and to the analyzed volume.

The number of detected recoil protons in the data was (6330 ± 1280) events, in fair agreement with the predicted value of (5990 ± 70) events. We have estimated for the data a statistical error of 1.3% and an overall systematic uncertainty of 20.3% due to the following contributions: 17.1% to the hydrogen NIT content, 6.5% to the NIT density, 5.5% to the neutron fluence, and 6.6% to the shrinkage factor affecting the actual analyzed volume.

Figure 4 shows a data/MC comparison of the measured kinematic variables: proton range (R), scattering angle ($\cos \theta_{\text{Scat}}$), reconstructed neutron energy (E_n), and recoil-proton energy (E_p) in head-on collisions ($\cos \theta_{\text{Scat}} > 0.98$). They show a very good agreement both in normalization and in shape. The small excess around $\cos \theta_{\text{Scat}} = 1$ is expected to be due to the scattering from some materials close to the beam line, which was not described in the simulation. Figure 4(c) reports the neutron energy reconstructed through the recoil-proton energy and the scattering angle, with a peak value at (864 ± 46) keV, consistent with the exposure energy. The obtained energy resolution is $\Delta E_{n, \text{FWHM}}/E_n = 0.31$ for 880 keV neutrons, comparable to the value of 0.42 measured in the previous calibration run for 540 keV neutrons [4].

Since most of the protons are scattered at a small angle, the orientation of NIT film adopted in the exposure resulted in a higher detection efficiency. However, as described in Sec. II B, since the accuracy in the Z coordinate is worse than for the other coordinates, a dependency of the detection efficiency is expected on the Z inclination (θ_z). This is particularly true for short-range tracks. The estimated angular dependency of the detection efficiency is reported in Fig. 5, separately for tracks with ranges within (red) and above (blue) $4 \mu\text{m}$.

In order to bring the misidentification of dust events to a negligible level, a displacement between start and end points

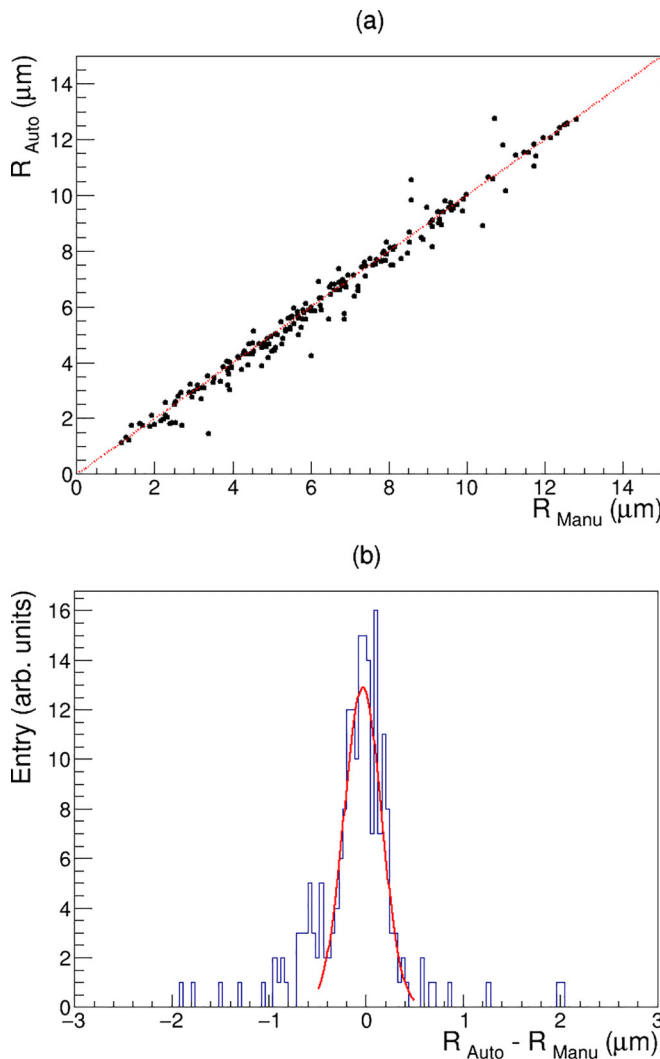


FIG. 3. (a) Correlation between manual and automated measurements of the proton range; red dotted line corresponds to equal values. (b) Distribution of the difference between manual and automated range measurements.

of the track in the horizontal direction was required to be larger than $1 \mu\text{m}$. This is reported hereafter as a 2D range cut. The detection efficiency gets lower for short vertical tracks once this cut is applied. The angular dependence of the detection efficiency in Fig. 5 was fitted with a sigmoid function (dash-dotted line).

IV. NEUTRON MEASUREMENT AT THE LNGS SURFACE LABORATORY

We have conducted a run at the LNGS surface laboratory to measure environmental neutrons, given that γ rays do not constitute a background in our analysis.

A. Experimental setup

NIT films were produced at the NEWSdm facility in Hall-F of the Gran Sasso underground, as shown in Fig. 6. NIT emulsion was produced in the facility, washed with ultrapure

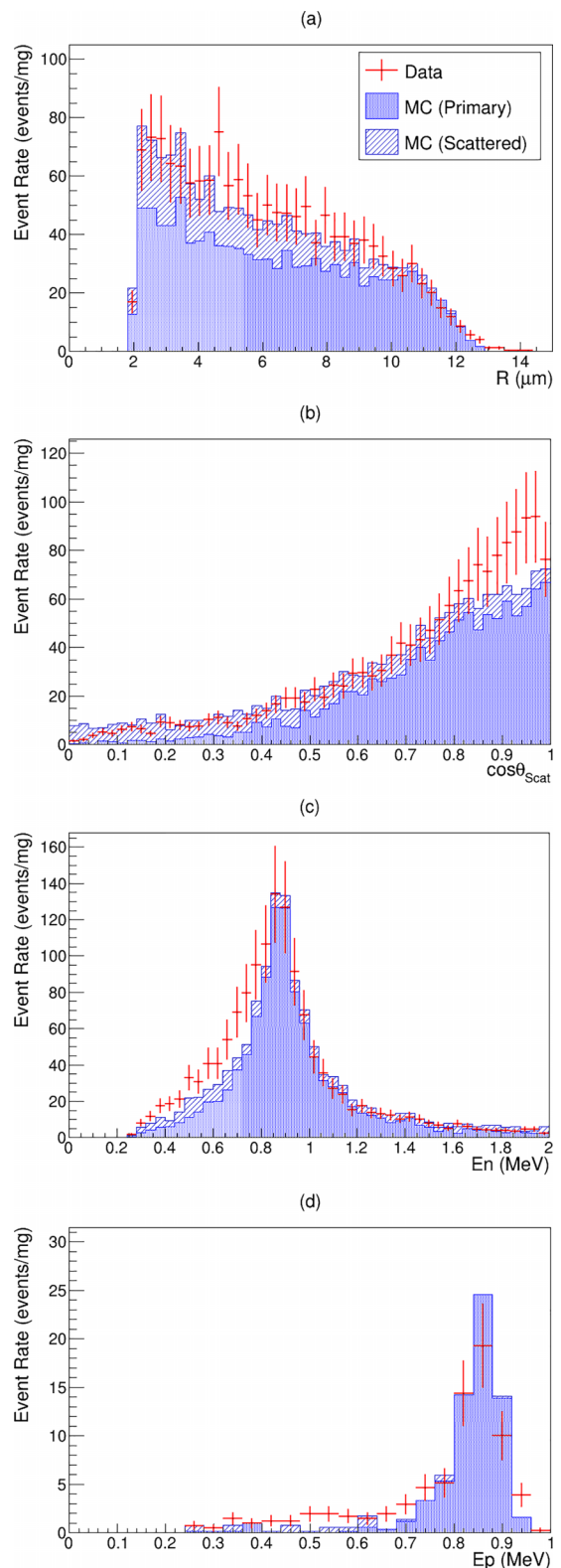


FIG. 4. Comparison between data (red) and MC simulation (blue) for the 880 keV monochromatic neutron exposure. For the simulation, primary and scattered neutrons are represented by blue filled and shaded histograms, respectively. (a) Proton range, (b) scattering angle, (c) reconstructed neutron energy using Eqs. (1) and (2), (d) recoil-proton energy of head-on collisions.

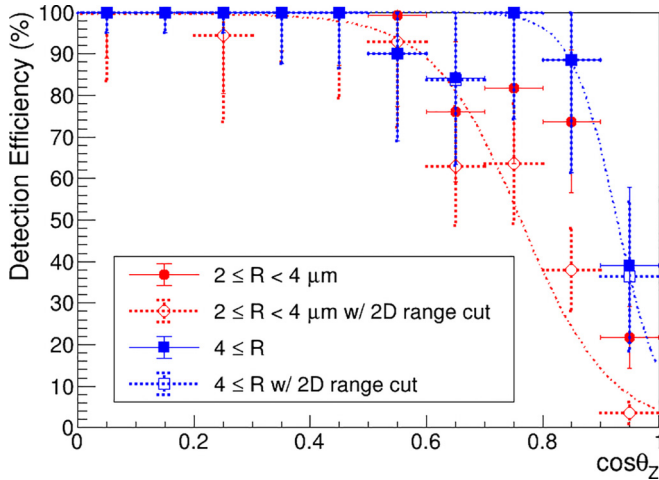


FIG. 5. Angular dependency of the detection efficiency for proton tracks induced by 880 keV monochromatic neutron scattering. Open symbols show the detection efficiency after a 2D range cut is applied, as described in the text.

water (called noodle washing) to remove Na^+ and NO_3^- ions, poured on a COP base and dried for one day, then the film became sensitive to tracks. After that, the films were dipped in a sodium sulfite solution of 0.0397 mol/L for their halogen-acceptor sensitization [15] and dried for another day. These

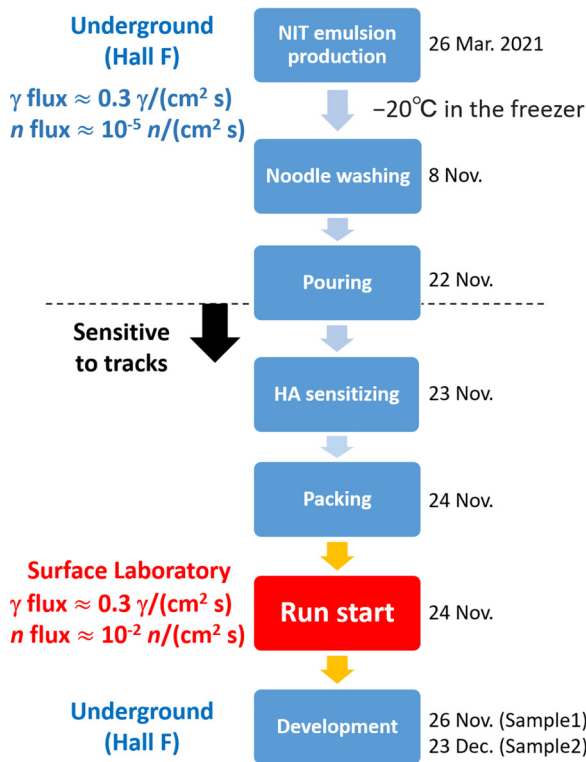


FIG. 6. Experimental procedure for the environmental neutron measurement at the LNGS surface laboratory. NIT film production and development were conducted in the underground facility. γ -ray and neutron fluxes are estimated by [3,11–14] for both underground and on the surface.

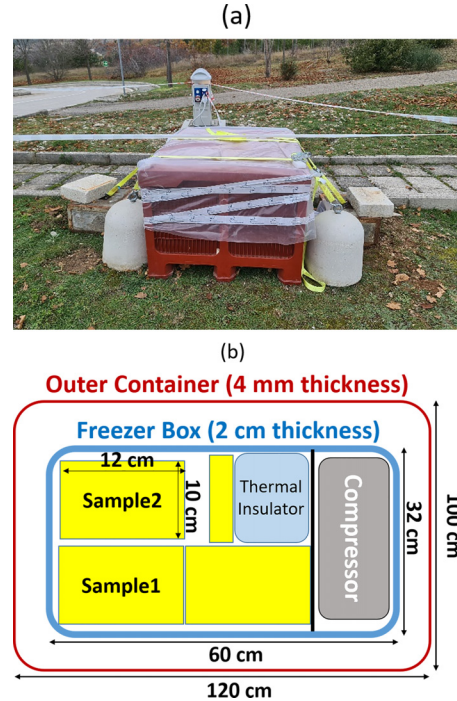


FIG. 7. Experimental setup for the environmental neutron measurement at the LNGS surface laboratory. (a) Picture of the setup soon after its installation. (b) Schematic top view of the inner part of the container box.

samples prepared underground were transported to the surface laboratory and installed in a portable freezer box located outdoor, as shown in Fig. 7. The thickness of the plastic containers was 4 mm for the outer container and approximately 2 cm for the portable freezer box. Samples were installed for up to 29 days with stable temperature at -20°C to suppress the fading effect as described in Sec. III. Table II shows the details of the two samples used in the measurement. Sample 1 was exposed for two days while Sample 2 was kept for

TABLE II. Details of the experimental setup.

	Sample 1	Sample 2
Surrounding environment	Portable freezer box (outdoor)	
Altitude	1400 m	
Expected angle-integrated flux of atmospheric neutron in 0.25 – 10 MeV (assumed water fraction in ground as 20%) [13,14]	$9.0 \times 10^{-3} \text{ n}/(\text{cm}^2 \text{ s})$	
Operation temperature	-20°C	
Run start date	24 Nov. 2021	
Preparation time in underground (days)	2	2
Exposure time (days)	2	29
Installation direction	Horizontal	
Analyzed area (cm^2)	46.7	99.4
Analyzed mass (g)	0.65	1.35

29 days at the Gran Sasso surface laboratory. The preparation of both samples took two days and it was carried out in the underground laboratory.

Considering that γ -ray flux at LNGS is around $0.3 \text{ } \gamma/(\text{cm}^2 \text{ s})$ both underground [11,12] and on the surface [13,14], the accumulated γ -ray densities in Sample 1 and Sample 2 are estimated to be $1 \times 10^5 \text{ } \gamma/\text{cm}^2$ and $8 \times 10^5 \text{ } \gamma/\text{cm}^2$, respectively. These levels are negligible, because our tracking analysis has a γ -ray rejection power at the level of $5 \times 10^7 \text{ } \gamma/\text{cm}^2$, as described in Sec. II B. In addition, the neutron flux underground is expected to be three orders of magnitude lower than on the surface [3], hence the NIT film production underground can be considered as a control sample for surface neutron measurement. Sample 1 is considered as the reference to study the initial level of radioactivity integrated in the sample. In order to extract the neutron rate, we subtract the rate measured in Sample 1 from the one measured in Sample 2 in the analysis and consider 27 days as the exposure time.

B. Event selection

In order to select neutron-induced proton recoil tracks, we require that both start and end points of the tracks are within the inner fiducial volume, which excludes the $10 \text{ } \mu\text{m}$ from the top and $5 \text{ } \mu\text{m}$ from the bottom of the emulsion. This is meant to reject external α rays due to ^{222}Rn from the air and from the ^{238}U or ^{232}Th radioactivity in the base materials. Events passing the fiducial volume cut are shown in Fig. 8 and are classified as single-prong [Fig. 8(a)] or multiprong [Fig. 8(b)] events, according to the track multiplicity at the vertex.

The intrinsic radioactivity from the ^{238}U and ^{232}Th decay chains in the NIT were measured γ -ray by a germanium detector [16] to be 6 mBq/kg for ^{228}Th and 0.8 mBq/kg for ^{226}Ra , and most of the α rays produced show a multiprong vertex. A typical example is the Th star [17], emitting five α rays in the decay process from ^{228}Th to ^{208}Pb . Inelastic scattering events by high-energy neutrons are also observed as multiprong, with short-range recoil nuclei and spallation fragments.

In this study, we focused on neutron elastic scattering, and only single-prong events are retained for the analysis. However, α rays might produce a single-prong event when there is a contamination from ^{214}Po (7.687 MeV) or ^{210}Po (5.304 MeV). Their track ranges in NIT are approximately $43 \text{ } \mu\text{m}$ and $24 \text{ } \mu\text{m}$, respectively (see Appendix B, C). Therefore, in this study, we set an upper limit for track range of $14 \text{ } \mu\text{m}$, which corresponds to the proton energy of 1 MeV , and analyze only recoil protons of $2\text{--}14 \text{ } \mu\text{m}$ ($0.25\text{--}1 \text{ MeV}$ in proton energy). The background is therefore negligible in this region. Figure 9 shows the detectable neutron energy spectrum, mostly in the range between 0.25 and 10 MeV , which reflects the cuts applied in the proton range measurement.

In addition, nitrogen contained in the NIT as a mass fraction of $(3.7 \pm 0.3)\%$ also produce a small fraction of signal, because the $^{14}\text{N}(n, p)^{14}\text{C}$ reaction emits protons with an energy of 0.58 MeV ($6.5 \text{ } \mu\text{m}$ in track range) when thermal or epithermal neutrons are captured by nitrogen [18].

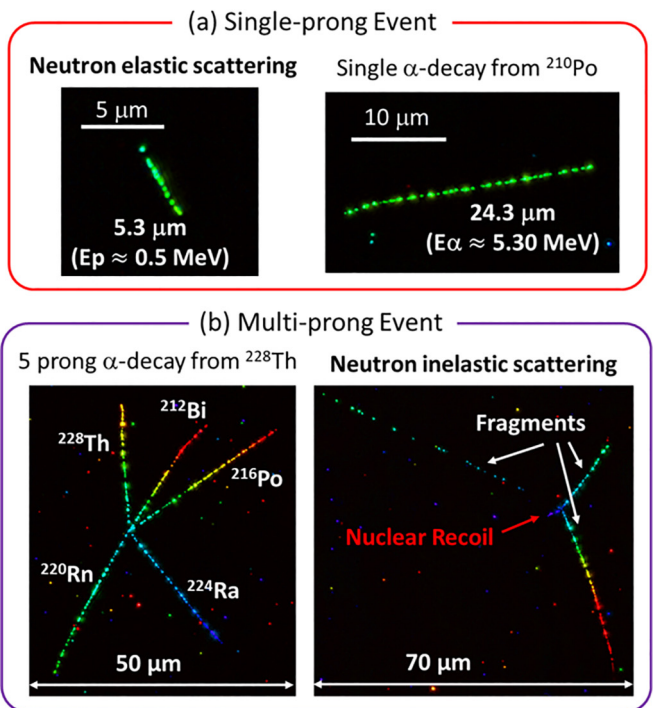
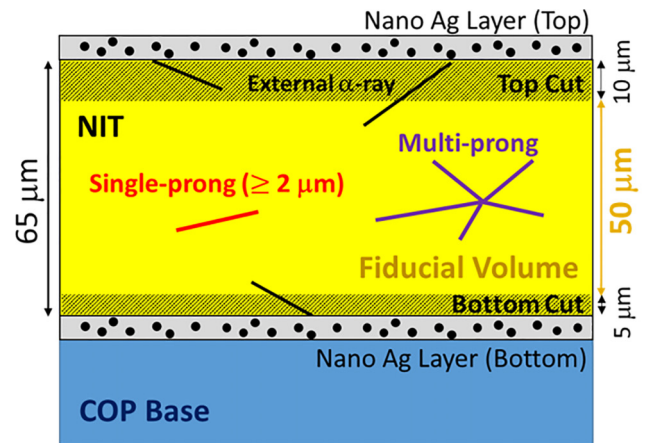


FIG. 8. Topological event classification: (a) Single-prong and (b) Multiprong events after fiducial volume cut. Colored scale in images corresponds to the Z coordinate, as shown in Fig. 1.

C. Result

Figure 10 shows the range distribution measured in Sample 1 and Sample 2. The number of detected events was (36 ± 7) events/g in Sample 1 and (336 ± 16) events/g in Sample 2, with a significant increase due to the exposure time, as expected. These events are essentially only protons produced in the neutron scattering, given the negligible background.

A MC simulation based on GEANT4 was carried out to compare the neutron flux and energy spectrum originated by atmospheric muons. We considered the neutron spectrum at the LNGS surface laboratory expected by the PARMA [19] model using the cosmic ray spectrum prediction software of EXPACS [13,14], which is published by a group of the Japan Atomic Energy Agency (JAEA). The simulation accounts for a thickness of 4 mm of the container and of 2 cm of the

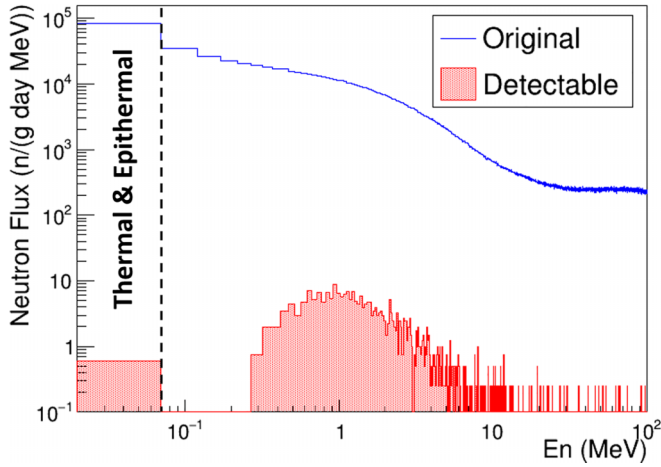


FIG. 9. Detectable neutron spectrum in NIT with 1 (g day) exposure at LNGS surface laboratory estimated by a MC simulation based on GEANT4. The blue line is the original energy of the incident neutrons, and the red filled histogram is the neutron spectrum accounting for the selection and the detection efficiency in this analysis. Below 100 keV is contribution from the $^{14}\text{N}(n, p)^{14}\text{C}$ reaction.

portable freezer box. Neutrons were generated from outside the container considering the zenith angular dependency predicted by the PARMA model.

Figure 11 shows the measured distributions of the recoil proton energy (E_p), plane angle (ϕ), and zenith angle ($\cos\theta_{\text{zenith}}$) in the data Sample 2 and the comparison with the MC simulation. The data of Sample 1 were subtracted from Sample 2 to obtain an equivalent exposure of 27 days. The number of events in the proton energy range between 0.25 and 1 MeV was found to be $[11.1 \pm 0.6(\text{stat.}) \pm 2.4(\text{sys.})]$ events/(g day) in the data and (13.2 ± 0.4) events/(g day) in the simulation. The number of detected events is consistent with the neutron flux predicted by the PARMA model, and the energy spectrum and directional distribution also show a good agreement. Consequently, we obtained the measured

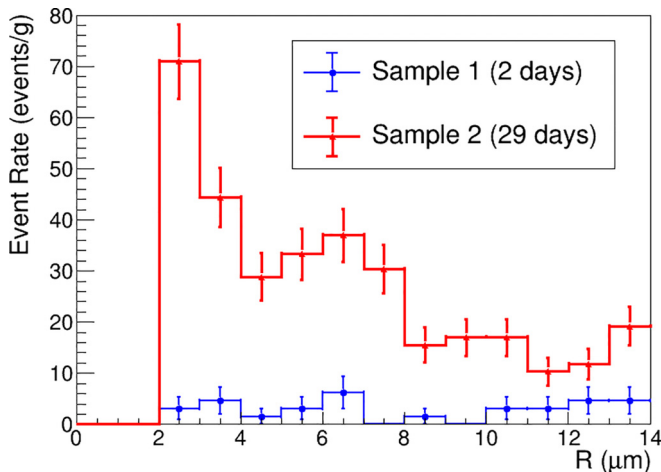


FIG. 10. Range distribution of recoil protons in the sub-MeV region for Sample 1 (two days, blue) and Sample 2 (29 days, red) samples at LNGS.

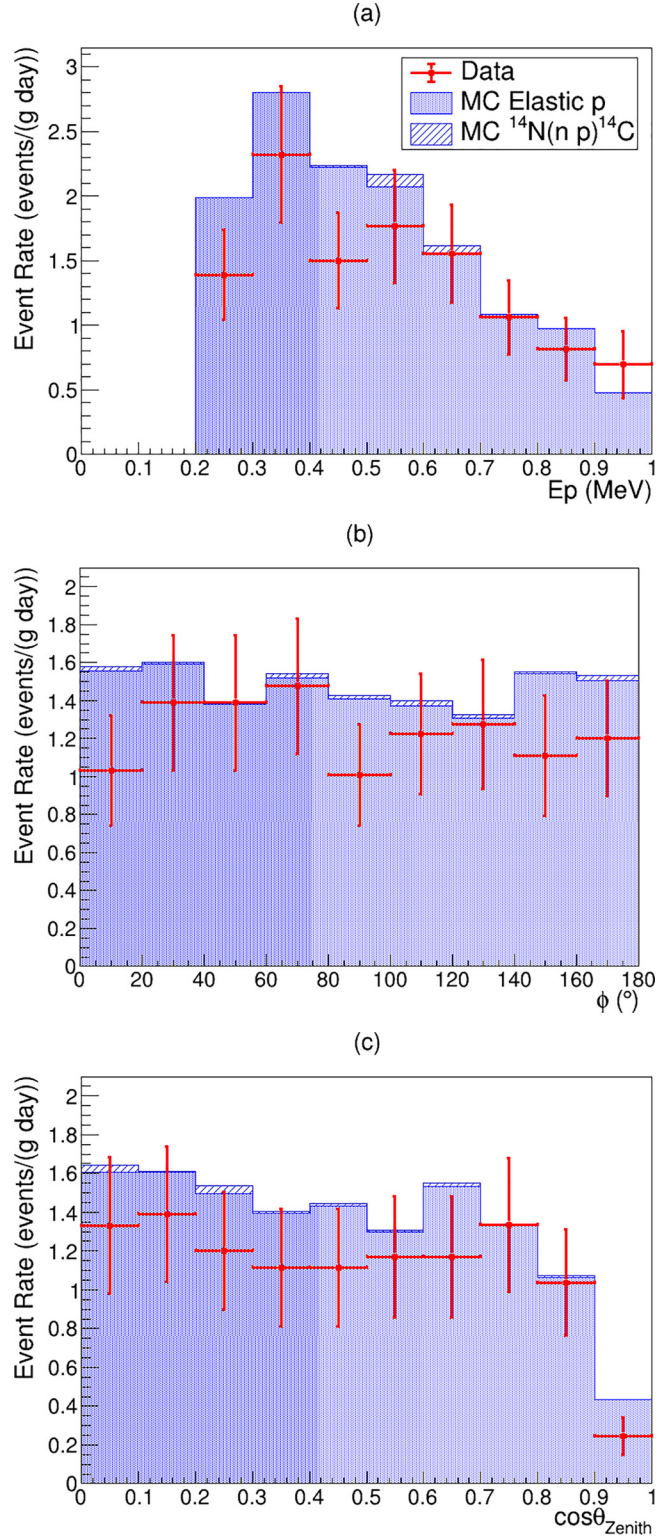


FIG. 11. Sub-MeV neutron measurement results after subtracting the data of Sample 1 from Sample 2 for an equivalent exposure of 27 days. For the MC simulation, neutron signals of elastic scattering and $^{14}\text{N}(n, p)^{14}\text{C}$ reaction are represented by blue filled and shaded histograms. The detection efficiency reported in Fig. 5 was applied to the MC simulation. (a) Proton energy spectrum, (b) plane angle, and (c) zenith angle.

neutron flux as $(7.6 \pm 1.7) \times 10^{-3} n/(\text{cm}^2 \text{ s})$ in the proton energy range between 0.25 and 1 MeV (corresponds to neutron energy range between 0.25 and 10 MeV).

V. PROSPECTS

In this study, we showed that the measured recoil proton energy spectrum is consistent with the prediction made by the PARMA model. In the future, one could use a collimator to determine the incoming neutron direction, thus reconstructing the neutron energy from the proton recoil energy and its scattering angle, as shown in Sec. III. Another way is to reconstruct the neutron energy by using the unfolding method with only the proton energy. In the latter case, a large statistical sample with a wide range of proton energies is needed and the systematic uncertainty due to the surrounding material has to be minimized.

We plan to extend this measurement to higher energies. This requires us to improve the microscope scanning speed, given the lower flux, and to reduce the background from α rays (see Appendix C). The increase of the scanning speed will also allow us to extend the measurement to the neutrons at LNGS underground where the flux is expected to be three orders of magnitude lower than on the surface. The high accuracy of the emulsion in topological analyses allows extending the analyzed sample to events with multiple fragments, thus becoming sensitive also to inelastic neutron scattering, relevant for energies of a few hundred MeV.

Since this neutron detection technique uses the hydrogen content of the emulsion, it also paves the way to the search for low-mass DM. Even though DM masses below $1 \text{ GeV}/c^2$ are plausible for the galaxy formation mechanism, they have remained unexplored due to technical difficulties. Recently, cosmic ray boosted dark matters (CR-DMs), i.e., DM accelerated by collisions with protons and helium nuclei in the galaxy, was suggested as one of the DM investigation methods [20]. CR-DMs is a natural consequence of the DM interactions with nucleons, as foreseen by the standard WIMP model. They are predicted to have low mass and a speed higher than the escape velocity of the galaxy: their orientation should preferentially be from the galactic center because of their acceleration mechanism [21]. By applying the neutron measurement technique with NIT, it is possible to search for low-mass dark matter such as CR-DMs with a directional sensitivity.

VI. CONCLUSION

For the environmental neutron measurement, we first upgraded the submicrometric three-dimensional tracking system and achieved an analysis speed of 250 g/(year machine). Then, we calibrated the performance of this system through the analysis of a sample exposed to monochromatic 880 keV neutrons at the temperature of -26°C and we reported a very good agreement of all the kinematic variables relevant for the neutron elastic scattering. The neutron energy, reconstructed by the recoil proton energy and its scattering angle, was measured to be $(864 \pm 46) \text{ keV}$ at the peak value, and its accuracy

was $\Delta E_{n,\text{FWHM}}/E_n = 0.31$ with the automated measurement accuracy.

We then performed the environmental neutron measurement at the LNGS surface laboratory. The neutron flux in the proton energy range between 0.25 and 1 MeV was measured to be $(7.6 \pm 1.7) \times 10^{-3} n/(\text{cm}^2 \text{ s})$, in good agreement with the prediction by the PARMA model. The uncertainty of this measurement is mainly due to the systematic error associated with the hydrogen content in the films, which should be measured with higher accuracy for future and more accurate neutron measurements.

We intend to extend this measurement at the LNGS surface laboratory in the MeV region, by lowering the background contamination from the α -ray tracks in the production process and by increasing the statistics. We also plan to perform neutron measurements in the LNGS underground laboratory.

ACKNOWLEDGMENTS

This work was supported by the Japan Society for the Promotion of Science (JSPS) KAKENHI Grants No. JP18H03699, No. JP19H05806, and No. JP22J01541. This work was also carried out by the joint usage/research program of the Institute of Materials and Systems for Sustainability (IMaSS), Nagoya University. This research was carried out in the frame of the STAR Plus Programme, financially supported by University of Naples “Federico II” and Compagnia di San Paolo. Monochromatic neutron source was supported by Dr. Tetsuro Matsumoto and Dr. Akihiko Masuda of the National Metrology Institute of Japan (NMIJ), the National Institute of Advance Industrial Science and Technology (AIST).

APPENDIX A: LOW-TEMPERATURE CONTROL SYSTEM

We developed a portable cooling system to perform neutron exposure experiments at low temperature. We used SC-UD08 Stirling cooler manufactured by TWINBIRD Corporation, which has a cooling capacity of approximately 15 W at -100°C and 60 W at -20°C at maximum output, and its output can be controlled by a 1–5 V input voltage. For the control of Stirling cooler, we also developed temperature control system using the SoC-FPGA (DE10-nano), as shown in Fig. 12(a).

First, a platinum resistance thermometer (P0K1.232.6W.B.007), which has good temperature characteristics at low temperatures, is used to convert the sample temperature to a resistance value, then the Wheatstone Bridge circuit converts resistance to voltage. This voltage is digitally converted by the AD converter (LTC2308) when a command is received from the CPU, and the data is written to the shared memory. After the digital conversion, the CPU accesses the data on the shared memory to monitor the current temperature, and determines the control voltage by PID control as described below and sends the data to the DA converter (MCP4921) to set the control voltage of the Stirling cooler.

In the PID control, the voltage for the Stirling cooler (V_{Control}) is determined by the following equation with the

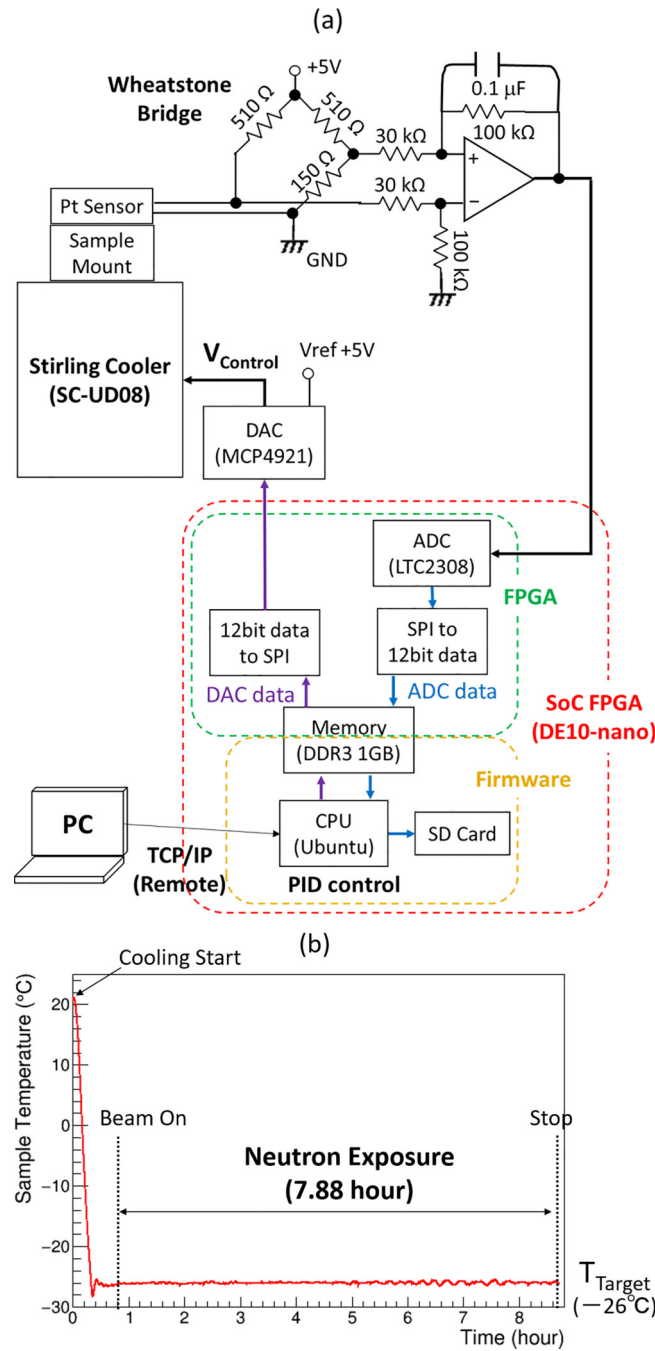


FIG. 12. (a) Temperature control system using Stirling cooler (SC-UD08). (b) Temperature profile of a sample during the neutron exposure at AIST. The sample reached the target temperature of $-26\text{ }^{\circ}\text{C}$ in approximately 20 min. Neutron exposure was carried out for 7.88 h under stable temperature.

target temperature T_{Target} and the temperature $T(t)$ at time t :

$$V_{\text{Control}} = K_p \Delta T + K_i \int_0^t \Delta T dt + K_d \frac{dT(t)}{dt}, \quad (\text{A1})$$

where $\Delta T = T(t) - T_{\text{Target}}$, and the coefficients K_p , K_i , and K_d were obtained by the ultimate sensitivity method [22] as 0.18, 7.8×10^{-4} , and 10, respectively. A series of

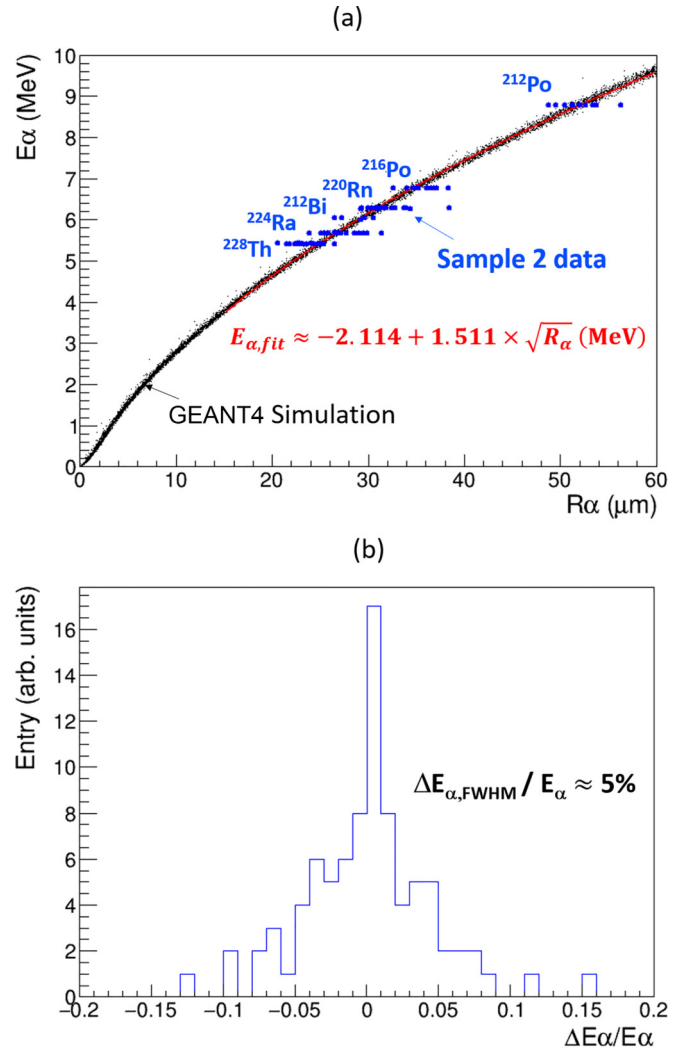


FIG. 13. (a) Correlation between α -ray range and energy. Blue plots are data using the Th star events detected in Sample 2, black plots are the predictions from the GEANT4 simulation, and the red line is the best-fit function from the data. (b) α -ray energy resolution obtained from the measured range.

feedback control by PID is performed at 5 s intervals. Figure 12(b) shows the actual temperature profile of the NIT sample during the 880 keV monochromatic neutron exposure at AIST.

APPENDIX B: ACCURACY OF α -RAY ENERGY MEASUREMENT

To identify the α -ray source, the energy calibration was performed using the Th star events found from Sample 2 of LNGS run. Five-prong events can be easily identified as Th star since they are produced by the decay of ^{228}Th to ^{208}Pb during the run because of their long lifetime. In addition, these tracks can be used to calibrate the correlation between range and decay energy, because it is easy to determine which track corresponds to which decay. The correlation between measured range and decay energy is shown in Fig. 13 for decays fully contained within the emulsion. The following

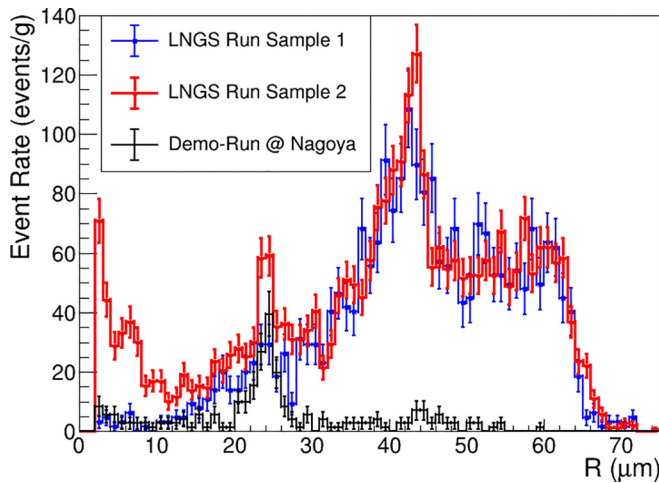


FIG. 14. Full-range distribution for Sample 1 (two days, blue) and Sample 2 (29 days, red) samples. A demo-run (black) performed at Nagoya University (Japan) with 31 days exposure for the background study shows that the background due to longer range events (in the MeV region) is much lower than at LNGS, due to a different NIT production protocol.

formula can be used to estimate the α -ray energy (E_α) in the range between 4 and 10 MeV.

$$E_\alpha \approx -2.114 + 1.511 \times \sqrt{R} \quad (\text{MeV}). \quad (\text{B1})$$

APPENDIX C: MeV REGION

As described in Sec. IV B, in this study we have focused on the sub-MeV proton energy region to avoid α -rays background in the MeV region. The actual range distribution in the MeV region is shown in Fig. 14.

As a demonstration run to estimate the amount of background, we had performed similar measurements inside a building at Nagoya University in Japan, where the neutron flux was lower than at LNGS, with 31 days exposure. In the demo run, a peak at $(24.3 \pm 0.4) \mu\text{m}$ corresponding to an α -ray energy of $(5.30 \pm 0.08) \text{ MeV}$ was observed and it was identified as α rays from ^{210}Po with a relatively long half-life. In principle, the MeV region can be analyzed by avoiding this region.

However, for the LNGS run reported in Fig. 14, we can observe different time-independent contributions in the range between 30 and 65 μm . We noticed that some of these tracks show low brightness of their reconstructed grains. Figure 15 shows the α -ray energy distribution separated in two categories: normal [Fig. 15(a)] and low [Fig. 15(b)] brightness. In the normal brightness track sample, α -ray tracks from ^{214}Po (daughter nucleus of ^{222}Rn) were observed around

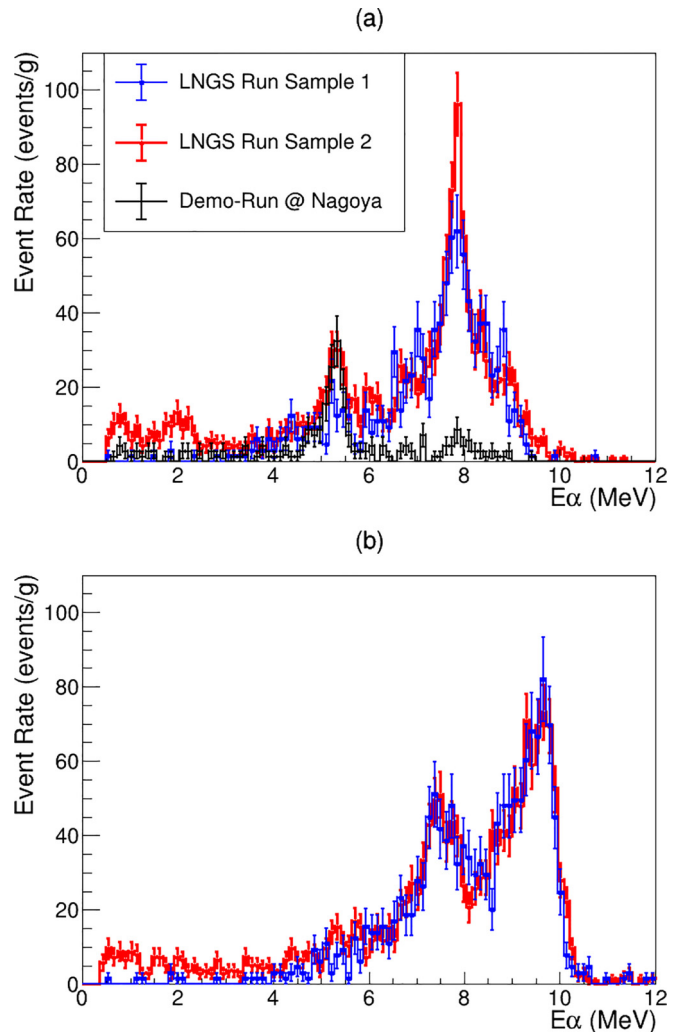


FIG. 15. α -ray energy spectrum computed by Eq. (4) for Sample 1 (two days, blue) and Sample 2 (29 days, red) samples at LNGS and for a demo run (31 days, black) at Nagoya. (a) Normal and (b) low brightness tracks.

$(7.81 \pm 0.12) \text{ MeV}$. In the low brightness track sample, the distribution can be explained by assuming that they originate from ^{214}Po contamination during the drying process. Indeed, during drying, the AgBr:I crystals are more dispersed due to the higher water content, which turns into a lower sensitivity to α -ray tracks and, hence, to a lower brightness. Their length is also longer because of the lower mass density of the film in this phase. After drying, NIT films shrink in the Z direction due to the evaporation of water, which turns into a wider-range distribution.

We have already established a NIT production method with less contamination of ^{214}Po at the LNGS underground laboratory, which would allow performing neutron measurements with reduced MeV background in the future.

[1] G. Steigman and M. S. Turner, *Nucl. Phys. B* **253**, 375 (1985).

[2] D. N. Spergel, *Phys. Rev. D* **37**, 1353 (1988).

[3] A. Rindi, F. Celani, M. Lindozzi, and S. Miozzi, *Nucl. Inst. Meth. A* **272**, 871 (1988).

- [4] T. Shiraishi, I. Todoroki, T. Naka, A. Umemoto, R. Kobayashi, and O. Sato, *Prog. Theor. Exp. Phys.* **2021**, 043H01 (2021).
- [5] T. Naka, T. Asada, T. Katsuragawa, K. Hakamata, M. Yoshimoto, K. Kuwabara, M. Nakamura, O. Sato, T. Nakano, Y. Tawara, G. De Lellis, C. Sirignano, and N. D'Ambrossio, *Nucl. Inst. Meth. A* **718**, 519 (2013).
- [6] T. Asada, T. Naka, K. Kuwabara, and M. Yoshimoto, *Prog. Theor. Exp. Phys.* **2017**, 063H01 (2017).
- [7] N. Agafonova *et al.*, *Eur. Phys. J. C* **78**, 578 (2018).
- [8] T. Katsuragawa, A. Umemoto, M. Yoshimoto, T. Naka, and T. Asada, *JINST* **12**, T04002 (2017).
- [9] A. Umemoto, T. Naka, T. Nakano, R. Kobayashi, T. Shiraishi, and T. Asada, *Prog. Theor. Exp. Phys.* **2020**, 103H02 (2020).
- [10] H. Harano, T. Matsumoto, J. Nishiyama, A. Uritani, and K. Kudo, *AIP Conf. Proc.* **1099**, 915 (2009).
- [11] M. Haffke, L. Baudis, T. Bruch, A. D. Ferella, T. Marrodan Undagoitia, M. Schumann, Y.-F. Te, and A. van der Schaaf, *Nucl. Inst. Meth. A* **643**, 36 (2011).
- [12] D. Malczewski, J. Kisiel, and J. Dorda, *J. Radioanal. Nucl. Chem.* **295**, 749 (2013).
- [13] T. Sato, *PLOS ONE* **10**, e0144679 (2015).
- [14] T. Sato, *PLOS ONE* **11**, e0160390 (2016).
- [15] T. Tsutsumi, K. Morimoto, S. Kimura, T. Suzuki, T. Mitsuhashi, K. Kuge, and A. Hasegawa, *J. Imaging Sci. Technol.* **53**, 10507 (2009).
- [16] A. Alexandrov, T. Asada, A. Buonauro, L. Consiglio, N. D'Ambrosio, G. De Lellis, A. DiCrescenzo, N. Di Marco, M. L. Di Vacri, S. Furuya, G. Galati, V. Gentile, T. Katsuragawa, M. Laubenstein, A. Lauria, P. F. Loverre, S. Machii, P. Monacelli, M. C. Montesi, T. Naka, F. Pupilli, G. Rosa, O. Sato, P. Strolin *et al.*, *Astropart. Phys. A* **80**, 16 (2016).
- [17] G. G. Eichholz and F. C. Flack, *J. Chem. Phys.* **19**, 363 (1951).
- [18] D. M. Van Patter and W. Whaling, *Rev. Mod. Phys.* **29**, 757 (1957).
- [19] T. Sato, H. Yasuda, K. Niita, A. Endo, and L. Sihver, *Radiat. Res.* **170**, 244 (2008).
- [20] T. Bringmann and M. Pospelov, *Phys. Rev. Lett.* **122**, 171801 (2019).
- [21] S. F. Ge, J. Liu, Q. Yuan, and N. Zhou, *Phys. Rev. Lett.* **126**, 091804 (2021).
- [22] J. B. Ziegler and N. B. Nichols, *Trans. ASME* **64**, 759 (1942).